Analogue of electromagnetically induced transparency in square slotted silicon metasurfaces supporting bound states in the continuum

J. F. Algorri,[1,2,3] F. Dell'Olio,[4] P. Roldán-Varona,[1,2,3] L. Rodríguez-Cobo,[2] J. M. López-Higuera,[1,2,3] J. M. Sánchez-Pena,[5] V. Dmitriev,[6] and D. C. Zografopoulos[7,*]

[1] *Photonics Engineering Group, University of Cantabria, 39005 Santander, Spain*
[2] *CIBER-bbn, Instituto de Salud Carlos III, 28029 Madrid, Spain*
[3] *Instituto de Investigación Sanitaria Valdecilla (IDIVAL), 39011 Santander, Spain*
[4] *Department of Electrical and Information Engineering, Polytechnic University of Bari, 70125 Bari, Italy*
[5] *Department of Electronic Technology, Carlos III University, Madrid 28911, Spain*
[6] *Electrical Engineering Department, Federal University of Pará, CEP 66075-900 Belém, Brazil*
[7] *Consiglio Nazionale delle Ricerche, Istituto per la Microelettronica e Microsistemi (CNR-IMM), Roma 00133, Italy*
[*]dimitrios.zografopoulos@artov.imm.cnr.it

Abstract: In this work, a silicon metasurface designed to support electromagnetically induced transparency (EIT) based on quasi-bound states in the continuum (qBIC) is proposed and theoretically demonstrated in the near-infrared spectrum. The metasurface consists of a periodic array of square slot rings etched in a silicon layer. The interruption of the slot rings by a silicon bridge breaks the symmetry of the structure producing qBIC stemming from symmetry-protected states, as rigorously demonstrated by a group theory analysis. One of the qBIC is found to behave as a resonance-trapped mode in the perturbed metasurface, which obtains very high quality factor values at certain dimensions of the silicon bridge. Thanks to the interaction of the sharp qBIC resonances with a broadband bright background mode, sharp high-transmittance peaks are observed within a low-transmittance spectral window, thus producing a photonic analogue of EIT. Moreover, the resonator possesses a simple bulk geometry with channels that facilitate the use in biosensing. The sensitivity of the resonant qBIC on the refractive index of the surrounding material is calculated in the context of refractometric sensing. The sharp EIT-effect of the proposed metasurface, along with the associated strong energy confinement may find direct use in emerging applications based on strong light-matter interactions, such as non-linear devices, lasing, biological sensors, optical trapping, and optical communications.

1. Introduction

The use of dielectric metasurfaces (MS) has grown exponentially in recent years. In these structures, coupling and interference effects occur thanks to magnetic and electric resonant multipoles. These effects generate interesting optical phenomena with desirable properties that make dielectric MS suitable for numerous applications, for instance the precise control of light emission [1] or photoluminescence [2], polarization control [3,4], sensing [5,6], wave propagation control on microwave waveguides [7], highly-selective filtering [8–10], or applications based on the enhancement of nonlinear processes [11,12] among others.

Similarly, a lot of attention has been paid to the generation of electromagnetic induced transparency (EIT)-like effects in microresonators [13,14], guided-mode resonances [15,16], waveguides side-coupled to resonators [17,18], nanoscale plasmonic systems [19,20], and MS

[21–26]. In that case, the classical analogue of quantum EIT, which requires gas-phase three-level atoms, is replaced by coupling of a broadband bright mode resonator, which is accessible from free space, with a less-accessible or inaccessible narrowband dark mode resonator [21].

One of the most important characteristics of EIT is that strong light-matter interaction can be produced at the spectral region of the resonance in transmission. Contrary to plasmonic or metallic MS at which EIT Q-factors are limited by losses [27–35], some theoretical works on dielectric MS have shown ultra-high EIT Q-factors, in the ideal case of infinite transverse MS dimensions and lossless structures. These works are based, e.g., on toroidal dipolar responses [25] or trapped magnetic modes [26]. In the case of experimental reports, a value up to 500 (array size of 300×300 unit cells), has been demonstrated by using a unit cell consisting of two dielectric resonators [21]. Other recent reports have proposed the use of quasi-bound states in the continuum (qBIC) to achieve high-transmittance resonances with Q values of 18511 (array size of 27×27 unit cells) [36] and EIT-qBIC effect with $Q = 1000$ (array size of 15×15 unit cells) [37]. Such MS support a pure BIC state, namely with an infinite Q-factor, at the Γ-point of the first Brillouin zone. The main difference between them is that in the first case, the symmetry is broken by perturbing the geometry of the unit cell, [36], whereas in the second case, the emergence of the qBIC resonance is explained through Brewster-like mechanism [38], at which the excitation of a perpendicular dipole (either electric or magnetic) is forbidden at normal incidence [37].

In this work, we propose a novel type of MS based on the building block of square slot rings in a silicon wafer, which belongs to the so-called mesh-type MS configuration. The concept of the proposed MS is evolved from previous work, which however targeted sharp reflection resonances in a high-transmittance background [39]. For a certain height of the silicon layer where the MS is etched, a broad electric dipole bright resonance with zero transmittance at its center can be adjusted to occur at a target wavelength. Then, the symmetry of the square rings is broken by introducing a silicon bridge that interrupts the square slots, thus opening an access channel for coupling with the incident planewave and transforming the pure BIC states to qBIC with a finite Q-factor. The demonstrated qBIC-induced EIT effect occurs for normal wave incidence, contrary to the very recently introduced concept of qBIC-EIT dielectric metasurfaces, which was based on oblique incidence [37,38].

Following a detailed mathematical analysis, based on group theory and the symmetry adapted linear combination (SALC) method, we theoretically demonstrate that such slotted MS are capable of supporting several qBIC, whose symmetry properties are identified. The results are corroborated by finite-element eigenfrequency calculations. Moreover, the symmetry analysis provides useful selection rules in terms of the excitation of the qBIC resonances as a function of the linear polarization of the incident planewave. These rules are exploited to design both dual- and single-EIT resonances, which are switchable by changing the light polarization. As a result, by coupling the broad resonance to the qBIC, high-Q transparency peaks are observed in the form of Fano resonances. The quality factor of the EIT-qBIC resonances can be controlled by varying the size of the silicon bridge, which dictates their coupling with the impinging planewaves.

Furthermore, we also show that one of these qBICs manifests as a resonance-trapped mode with very high Q-factor at certain values of the silicon bridge. The relatively large dimension of the silicon bridge along with the inherent robustness of resonance-trapped modes to small geometrical variations significantly facilitates the fabrication of the metasurface. Finally, as an example of applications, the sensitivity of the qBIC resonant wavelengths on the refractive index of the surrounding material is calculated to evaluate its performance as a refractometric sensor e.g. for gas or bio-sensing. Other possible applications include systems based on strong light-matter interaction, such as non-linear, lasing, or light-trapping. In addition, given the low-dispersion of silicon and its mesh-type structure, the MS could directly find use in lower-frequency applications, e.g. in the THz spectrum, including the possibility to work in a free-standing configuration.

2.   Metasurface geometry and symmetry analysis

2.1.   Metasurface layout

The proposed MS is composed of a periodic array of square slot rings etched in a thin silicon layer on top of a glass substrate, as shown in Fig. 1. The structural parameters of the MS consist in the ring inner width w, the slot width s, the distance between adjacent rings g, and the silicon layer thickness h. The pitch of the periodic array, namely the size of the unit cell, equals $P = w + g + 2s$.
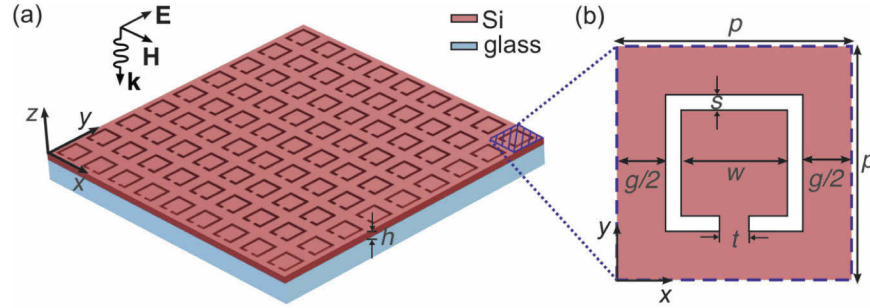

Fig. 1. (a) Schematic diagram of the investigated all-dielectric slot MS. A periodic array of square slot rings is etched in a thin silicon layer of thickness h. The MS lies on a semi-infinite glass substrate. (b) Top-view cross-section of the MS unit cell and definition of the pitch p and the geometrical parameters of the square slot, namely width s and inner size w. The symmetry of the structure is broken by introducing a silicon bridge of width t that interrupts the square slot.

To generate the qBIC, the slot ring is interrupted on one side by a narrow silicon bridge characterized by a width t, as shown in Fig. 1(b). The bridge breaks the symmetry of the structure along the y-axis, thus allowing for an y-polarized impinging planewave to couple to the qBIC modes, as it will be thoroughly discussed. In addition, the bridge establishes the continuity of the silicon layer, potentially permitting free-standing configuration for operation at lower frequencies, for instance in the THz spectrum using high-resistivity floating-zone silicon, which has very low absorption losses [40,41]. In the case here investigated, which targets operation in the near-infrared telecom-relevant spectrum, namely close to the wavelength of $\lambda = 1.55$ µm, the MS height h is in the order of a few hundred nanometers, so a glass substrate is considered as a supporting medium. The MS can be fabricated by standard nanofabrication processes, such as the deposition of the Si layer via low-pressure chemical vapor deposition (CVD) and the definition of the MS by electron beam lithography (EBL) or reactive ion etching [42]. Upscaling the MS to higher frequencies in the visible spectrum is also in principle possible by employing TiO_2 as the required high-index, transparent material. Indeed, TiO_2-qBIC metasurfaces have been recently experimentally investigated for lasing and exciton coupling [43,44].

2.2.   Symmetry analysis

The in-plane group of symmetry of the square unit cell shown in Fig. 1(b) without the silicon bridge, namely for $t = 0$, is C_{4v} in Schoenflies notations [45,46], with its elements shown in Fig. 2(a). The irreducible representations (IRREPs) of this group are given in Table 1. We consider the case of a planewave normally impinging on the discussed structure, which is described by the vectors of the electric field **E**, magnetic field **H** and the wave vector **k**. Our objective is to determine the existence of both symmetry-protected BIC and bright modes of the discussed MS and investigate their interaction with the field **E** of the incident wave, by employing a rigorous analytical tool, the SALC method.
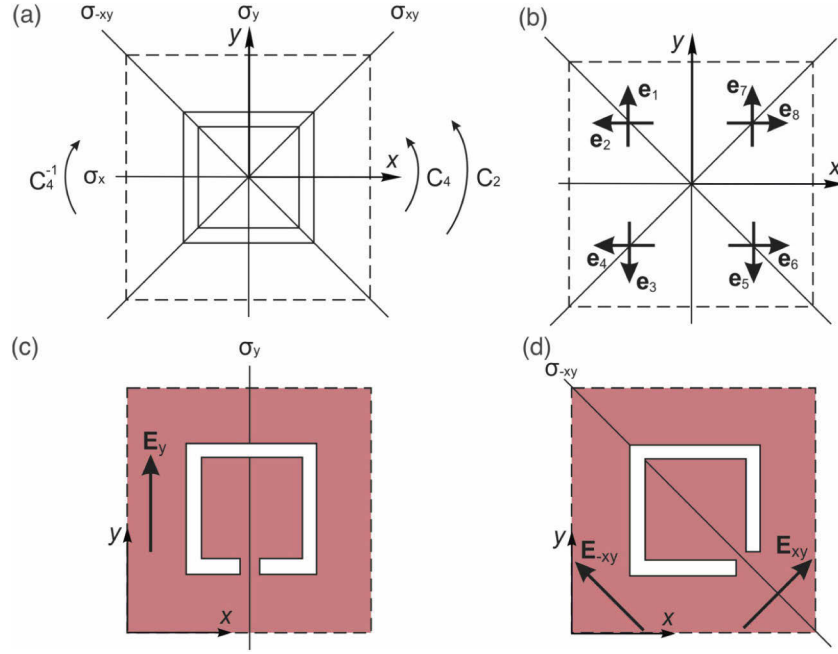
Fig. 2. (a) Nonperturbed unit cell of the MS with elements of its symmetry. (b) Basis for the SACL analysis of the nonperturbed unit cell (the square slot ring is not shown). (c,d) Symmetries of the perturbed MS unit cell: (c) plane of symmetry σ_y, group C_s^y, $\mathbf{E}_y$ is the exciting electric field; (d) plane of symmetry σ_{-xy}, group C_s^{-xy}, $\mathbf{E}_{xy}$ and $\mathbf{E}_{-xy}$ are the linear polarizations of the electric field for the excitation of the qBIC.

Table 1. IRREPs of group C_{4v}, E-field symmetry and mode types in the MS nonperturbed unit cell.

C_{4v}	e	C_2	C_4	C_4^{-1}	σ_x ($y = 0$)	σ_y ($x = 0$)	σ_{xy}	σ_{-xy}	Mode type of unit cell
A_1	1	1	1	1	1	1	1	1	dark radial
A_2	1	1	1	1	−1	−1	−1	−1	dark circular
B_1	1	1	−1	−1	1	1	−1	−1	dark quadrupole Q_1
B_2	1	1	−1	−1	−1	−1	1	1	dark quadrupole Q_2
E	$\begin{pmatrix} 1 & 0 \\ 0 & 1 \end{pmatrix}$	$\begin{pmatrix} -1 & 0 \\ 0 & -1 \end{pmatrix}$	$\begin{pmatrix} 0 & -1 \\ 1 & 0 \end{pmatrix}$	$\begin{pmatrix} 0 & 1 \\ -1 & 0 \end{pmatrix}$	$\begin{pmatrix} 1 & 0 \\ 0 & -1 \end{pmatrix}$	$\begin{pmatrix} -1 & 0 \\ 0 & 1 \end{pmatrix}$	$\begin{pmatrix} 0 & 1 \\ 1 & 0 \end{pmatrix}$	$\begin{pmatrix} 0 & -1 \\ -1 & 0 \end{pmatrix}$	bright D_x, dark Q_y bright D_y, dark Q_x

2.2.1. SALC approach to the unperturbed unit cell

A simplified schematic 2D description of the nonperturbed unit cell eigenmodes can be obtained by using the SALC method [47]. In our case, to represent the electric field distributions in the unit cell for every IRREP of the group C_{4v}, we have chosen eight unit vectors $\mathbf{e}_i$, ($i = 1, 2, \ldots 8$), which are shown in Fig. 2(b). The representations of the eigenmodes obtained by this method are summarized in Table 2, where the profile of the tangential components electric field on the $xy-$midplane of the silicon layer are also shown. The field profiles were calculated by eigenfrequency analysis for the periodic MS unit cell by using the finite-element method implemented in the software COMSOL Multiphysics. In the simulations, Floquet-Bloch periodic boundary conditions (PBC) were imposed at the lateral sides of the computational domain (*x-z* and *y-z* planes). Since we are interested here in identifying the symmetry-protected modes of the MS, i.e., for normal wave incidence (Γ point), the in-plane wavevector components of the

PBC were selected as $k_x = k_y = 0$. Two perfectly-matched layers, backed by scattering boundary conditions, were placed at distance from the metasurface along the z-axis in order to close the domain and allow for the accurate calculation of the complex eigenwavelengths of the system, which are reported in the first column of Table 2. The simulated structure corresponds to a MS with the following set of parameters: $h = 290$ nm, $w = 540$ nm, $g = 125$ nm, and $s = 30$ nm. A glass substrate is considered as the supporting medium, characterized by a refractive index of $n_g = 1.5$. It should be emphasized that the mode nomenclature in Table 2 corresponds only to reduced 2D description and does not always describe the entire 3D system.

The analysis presented in Table 1 reveals that the symmetric unit cell supports four dark, symmetry-protected BIC modes with IRREPs A_1, A_2, B_1, and B_2, respectively. The field profiles of these modes and their resonant wavelengths are shown in Table 2. All four dark modes are orthogonal to the field **E** because they belong to different IRREPs and, therefore, in the symmetry C_{4v} they can not be excited by the electric field of normally incident wave of any polarization. This can be also visually verified by inspecting the arrow plots in Table 2, which demonstrate that the four modes have zero electric field dipole moment in the xy-plane and hence they cannot couple to the incident planewave.

Furthermore, the first line of IRREP E describes two orthogonal modes, namely, D_x and Q_y, and the second line two other orthogonal modes, D_y and Q_x. Without perturbation, all of them have the same resonant frequency because they belong to the same IRREP. After rotation by 90°, the modes D_x and Q_y are transformed into D_y and Q_x, respectively. This defines the polarization-independence of modes E.

The dipole modes with components D_x and D_y are bright ones, i.e., they can be excited by the electric field **E** of the corresponding polarization. The quadrupole modes Q_x and Q_y are dark ones. Notice that in our discussion we consider only some principal features of the structure using 2D SALC description. To obtain a more detailed information, one needs a larger number of unit vectors and a 3D model.

2.2.2.   IRREP analysis of perturbation effects

In order to provide coupling of the excitation field with the dark/BIC modes of the structure, one needs to reduce the symmetry of the unit cell. In order to define the necessary reduction, we resort to Table 3 showing the symmetry degeneration of group C_{4v} [48].

Reduction of C_{4v} to its lower subgroup C_{2v} can be fulfilled for example, by changing the square slot ring of the unit cell to rectangular (group C_{2v}^v, the superscript v means vertical) or to rhombic one (group C_{2v}^d, the superscript d means diagonal). However, with such a reduction, IRREP A_1 (B_1) of C_{4v} is reduced to A_1 (A_2) of the group C_{2v}, but the 2D IRREP E of the field **E** is reduced to B_1 and B_2 of C_{2v}. Therefore, again, the fields of the discussed dark modes are orthogonal to the electric field **E** of the incident wave, thus excitation is impossible with this reduction. The four dark modes continue to be symmetry-protected BIC.

By further reducing the symmetry of the unit cell, one comes to the group C_s with only one plane of symmetry σ, a condition that allows excitation. Four orientations of the planes of symmetry are possible: two vertical planes σ_x, σ_y and two diagonal ones σ_{xy} and σ_{-xy}, as defined in Fig. 2(a). The two planes in the first pair are equivalent, the same is true for the second pair. Therefore in the following we shall consider only two of these planes, namely, σ_y and σ_{-xy}. The bridge position in Fig. 2(c) defines the plane σ_y. The plane σ_{-xy} can be provided by dislocation of the bridge to the corner of the square slot, as shown in Fig. 2(d).

In case of the vertical plane of symmetry σ_y, the dark modes A_1 and B_1 (A_2 and B_2) of IRREP A (B) in the reduced-symmetry group can be excited by the field $\mathbf{E}_y$ ($\mathbf{E}_x$), which belongs to the same IRREP (see Table 4). Following a similar analysis, in case of the diagonal plane of symmetry σ_{-xy}, the dark modes A_1 and B_2 (A_2 and B_1) require for their excitation a linear $\mathbf{E}_{xy}$ ($\mathbf{E}_{-xy}$) polarization of the incident wave (see Table 5) [49]. In the following we investigate the

Table 2. Eigenmodes of unit cell with C_{4v} symmetry in terms of vectors $\mathbf{e}_i$, as in Fig. 2(b). The field profiles refer to the in-plane component of the electric field $|\mathbf{E}_t|$, as calculated by eigenfrequency analysis of the MS symmetric unit cell.

IRREP	Eigenmode image	Field profile	Description
A_1 ($\lambda_{\text{eig}} = 1574.1$ nm)			Radial mode $\dfrac{1}{2\sqrt{2}}[(\mathbf{e}_1 + \mathbf{e}_2) + (\mathbf{e}_3 + \mathbf{e}_4) +$ $+ (\mathbf{e}_5 + \mathbf{e}_6) + (\mathbf{e}_7 + \mathbf{e}_8)]$
A_2 ($\lambda_{\text{eig}} = 1852$ nm)			Circular mode $\dfrac{1}{2\sqrt{2}}[(\mathbf{e}_1 - \mathbf{e}_2) - (\mathbf{e}_3 - \mathbf{e}_4) +$ $+ (\mathbf{e}_5 - \mathbf{e}_6) - (\mathbf{e}_7 - \mathbf{e}_8)]$
B_1 ($\lambda_{\text{eig}} = 1557.6$ nm)			Quadrupole mode Q_1 $\dfrac{1}{2\sqrt{2}}[(\mathbf{e}_1 - \mathbf{e}_2) + (\mathbf{e}_3 - \mathbf{e}_4) +$ $+ (\mathbf{e}_5 - \mathbf{e}_6) + (\mathbf{e}_7 - \mathbf{e}_8)]$
B_2 ($\lambda_{\text{eig}} = 1592.7$ nm)			Quadrupole mode Q_2 $\dfrac{1}{2\sqrt{2}}[(\mathbf{e}_1 + \mathbf{e}_2) - (\mathbf{e}_3 + \mathbf{e}_4) +$ $+ (\mathbf{e}_5 + \mathbf{e}_6) - (\mathbf{e}_7 + \mathbf{e}_8)]$
E, first line: E_{11} and E_{12} ($\lambda_{\text{eig}} = 1540.3$ nm)			Dipole D_x and quadrupole Q_y $\dfrac{1}{2}(\mathbf{e}_2 + \mathbf{e}_4 - \mathbf{e}_6 - \mathbf{e}_8)$ $\dfrac{1}{2}(\mathbf{e}_1 + \mathbf{e}_3 - \mathbf{e}_5 - \mathbf{e}_7)$
E, second line: E_{21} and E_{22} ($\lambda_{\text{eig}} = 1540.3$ nm)			Dipole D_y and quadrupole Q_x $\dfrac{1}{2}(\mathbf{e}_1 - \mathbf{e}_3 - \mathbf{e}_5 - \mathbf{e}_7)$ $\dfrac{1}{2}(\mathbf{e}_2 - \mathbf{e}_4 - \mathbf{e}_6 + \mathbf{e}_8)$

Table 3. Symmetry degeneration table of group C_{4v} [48].

C_{4v}	C_{2v}^v	C_{2v}^d	C_s^v	C_s^d
A_1	A_1	A_1	A	A
A_2	A_2	A_2	B	B
B_1	A_1	A_2	A	B
B_2	A_2	A_1	B	A
E	B_1, B_2	B_1, B_2	A, B	A, B

Table 4. IRREPs of group C_s^y, E-field symmetry and mode type.

C_s^y	e	$\sigma_y(x=0)$	**E**-field	Bright mode
A	1	1	$\mathbf{E}_y$	radial, Q_1, D_y, Q_x
B	1	-1	$\mathbf{E}_x$	circular, Q_2, D_x, Q_y

Table 5. IRREPs of group C_s^{-xy}, E-field symmetry and mode type.

C_s^{-xy}	e	σ_{-xy}	**E**-field	Bright mode
A	1	1	$\mathbf{E}_{-xy}$	radial, Q_2, D_{-xy}, Q_{xy}
B	1	-1	$\mathbf{E}_{xy}$	circular, Q_1, D_{xy}, Q_{-xy}

radial and the quadrupole Q_1 modes, as it will be demonstrated that these are involved in the target EIT-effect. We focus mainly on the symmetry-reduction scenario of Fig. 2(c) although some proof-of-concept results are provided for the case of diagonal symmetry of Fig. 2(d) as well.

3. Wave propagation studies and electromagnetically-induced transparency

3.1. Transmission spectra

The optical response, namely the transmittance spectra, of the MS is calculated by using Reticolo, an open-source electromagnetic solver based on the rigorous coupled wave analysis (RCWA) [50–52]. The RCWA relies on the computation of the eigenmodes in the layers of a stratified structure in a Fourier basis and a scattering matrix approach to relate the mode amplitudes in the different layers. It takes naturally into account the periodicity of the structure, here the two-dimensional MS, and finally calculates the diffraction efficiencies of all orders of the reflected and transmitted waves. Owing to the subwavelength MS pitch, there are no propagating diffraction orders, hence the software calculates the transmittance of the MS for both polarizations of the impinging planewave.

The MS structural parameters are selected so as to produce BIC resonances close to $\lambda = 1.55$ μm and inside the low-transmittance background spectrum stemming from coupling of the impinging planewave with the broad bright dielectric dipole mode, whose minimum is defined by a $\lambda/2$ resonance in the z-direction of the silicon layer of thickness h. Figure 3(b) shows the transmittance spectra for the symmetric MS for thickness values varying from $h = 240$ to 340 nm. The resonant wavelength changes almost linearly over h in the considered range with an average value of 2.4 μm/nm. The thickness of the silicon layer can be adjusted by, e.g., controlling the growth speed in CVD processes, which can be in the order of 1 Å/s.

The electric field profile at minimum transmittance, calculated for $t = 0$, is shown in the inset of Fig. 3(a) and it shows a dipole nature. Also shown is the relative field enhancement factor, defined as FEF= $|\mathbf{E}|/|\mathbf{E}_0|$, where $|\mathbf{E}_0|$ is the amplitude of the incident planewave. The FEF is low, since the bright mode shows a broad resonance with a Q-factor around 10. The calculations
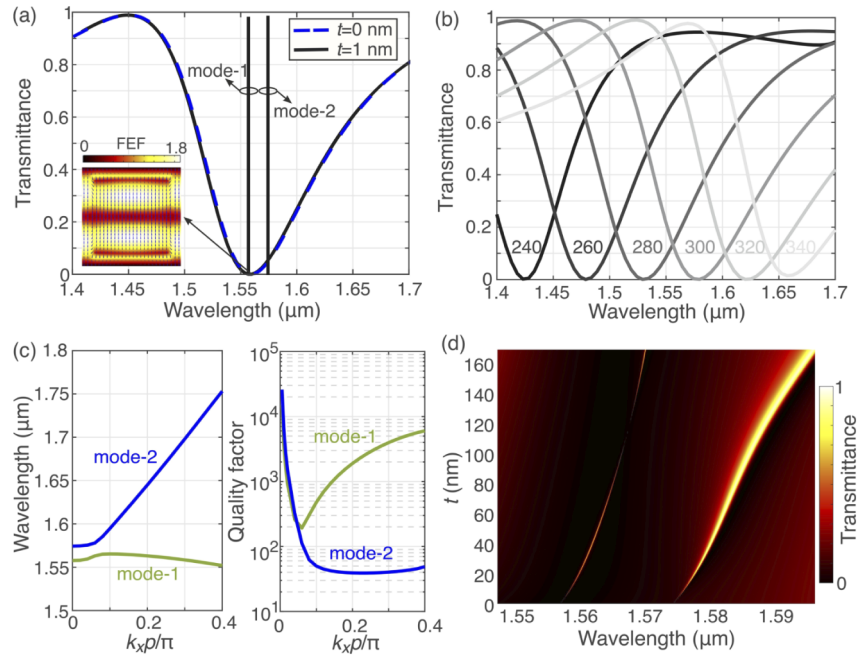
Fig. 3. (a) Transmittance of the MS for the symmetric ($t = 0$) and slightly asymmetric case ($t = 1$ nm), demonstrating the EIT effect and the excitation of two qBIC resonant modes. The inset shows the electric field profile at minimum transmittance of the broad bright electric dipole mode and the field enhancement factor. (b) Transmittance of the symmetric MS for silicon layer thickness varying between $h = 240$ and 340 nm. (c) Eigenwavelengths and Q-factors for the two qBIC modes along the $\Gamma \to X$ contour of the first Brillouin zone of the square periodic lattice of the MS. (d) Parametric study of the MS transmittance for silicon bridge width ranging from $t = 0$ to 170 nm.

refer to the set of parameters reported in Section 2.2.1. The minimum feature of the MS is the slot width of 30 nm, whose fabrication is feasible with EBL. In the calculations, the material dispersion of silicon was taken into account [53]. A *y*-polarized planewave is normally impinging on the MS, according to the definitions of Fig. 1.

In the absence of the silicon bridge the MS shows C_{4v} symmetry and its optical response is polarization-independent in the case of normal incidence. The MS transmittance spectrum is shown in Fig. 3(a). No sharp qBIC modes are observed, since these are symmetry-protected (pure) BIC. The symmetry-protected nature of the two BIC modes is further verified by calculating part of their band diagram by means of an eigenvalue analysis, where the k_x component of the Floquet-Bloch PBC varies from 0 to $0.4\pi/p$. The eigenwavelengths and the Q-factors of the two modes are shown in Fig. 3(c). Mode-2 exhibits much larger dispersion compared to mode-1. The Q-factor of both modes drops rapidly from the theoretically infinite value at the Γ point, which is indicative of symmetry-protected BIC modes.

The introduction of the silicon bridge enables coupling of *y*-polarized wave with the qBIC of the structure, identified in the analysis of Section 2.2. This is demonstrated in Fig. 3(a), where two sharp transmission peaks are observed inside the low-transmittance valley of the bright mode spectrum, calculated for $t = 1$ nm. The two modes, identified as mode-1 and mode-2, correspond to the radial and quadrupole Q_1 modes of the symmetry analysis (see Table 2) and they can both be excited by the $\mathbf{E}_y$ incident field (see Table 4). The resonant wavelength of mode-1 is close to that of the bright mode, which corresponds to zero transmittance, hence resulting in a

EIT effect. It was observed that a reduction of the slot width s, symmetrically with respect to Fig. 1(b), shifts the two qBIC resonances to higher wavelengths, as the fill-factor of silicon in the unit cell increases. Moreover, the two resonances become spectrally closer.

The properties of the qBIC modes depend strongly on the width t, which is investigated in Fig. 3(d). For increasing values of t the resonant wavelength of both modes shifts to higher values, as more silicon is introduced in the MS. However, the variation of the linewidth of the two qBIC modes shows different behaviour. It increases monotonically with t in the case of mode-2, whereas the linewidth of mode-1 increases initially, drops rapidly with a minimum at $t = 116$ nm and increases again for higher values of t. In order to gain more insight on the variation of the Q-factor of the two qBIC modes we resort again to the eigenfrequency calculations of the MS.

3.2. Quality factor analysis

Figure 4(a) shows the Q-factor of the two eigenmodes for a variation of the silicon bridge width in the range $0 < t \leq 200$ nm. The Q-factor for both modes diverges to infinity as $t \to 0$, which is a common feature of symmetry-protected BIC modes. By inspecting the electric field profiles of the two modes calculated for $t = 0$, as presented in Fig. 5 (also reported in Table 2), it can be observed that the in-plane distribution of the electric field (arrow plots) is antisymmetric with respect to both xz and yz-midplanes. Thus, by virtue of their symmetry, these modes cannot couple to a normally impinging planewave of any polarization, as discussed thoroughly in Section 2.2.
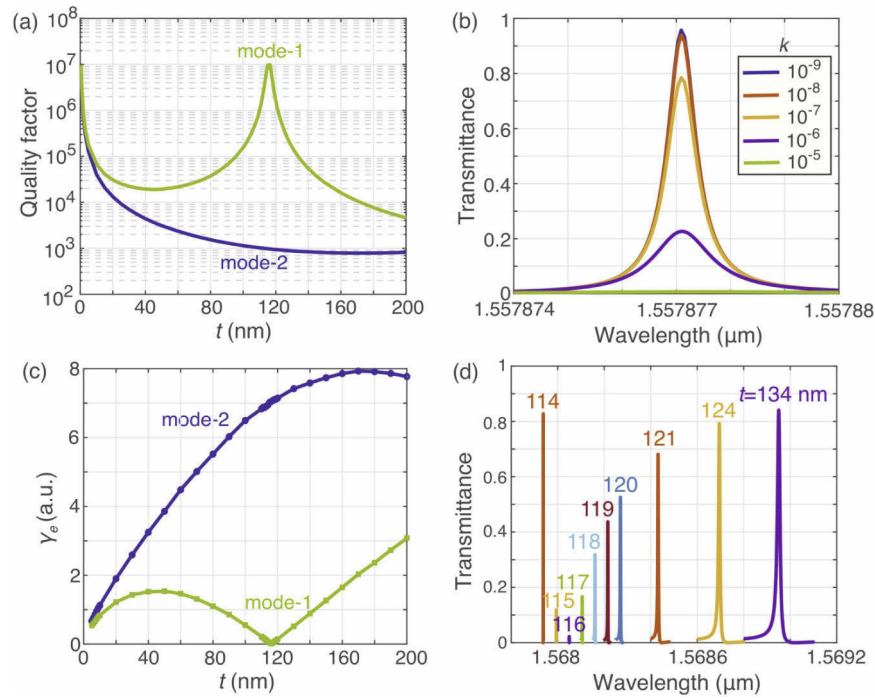

Fig. 4. (a) Q-factors of the two qBIC modes as a function of the silicon bridge width. (b) Transmittance spectra around the mode-1 resonance for $t = 1$ nm for various values of the silicon extinction coefficient. (c) Coupling coefficient of a normally impinging y-polarized planewave with the two qBIC modes. (d) Transmittance spectra around the mode-1 resonance for various values of the bridge width.
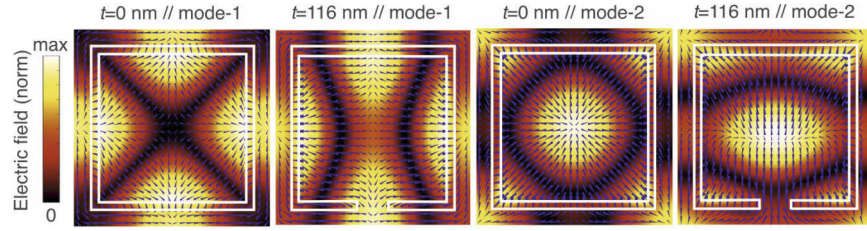
Fig. 5. Electric field profiles and arrow maps of the in-plane components of the electric field for the two BIC/qBIC eigenmodes calculated at the midplane of the slotted rings for $t = 0$ and $t = 116$ nm by eigenfrequency analysis. The corresponding eigenwavelengths are: $\lambda_{t=0}^{\text{mode-1}} = 1557.7$ nm, $\lambda_{t=0}^{\text{mode-2}} = 1573.4$ nm, $\lambda_{t=116}^{\text{mode-1}} = 1568.2$ nm, and $\lambda_{t=116}^{\text{mode-2}} = 1586.2$ nm.

Although theoretically arbitrarily high Q-factor values are possible at $t \to 0$, due to the suppression of radiative losses, in practice the maximum achievable Q-factor is mainly limited by nonradiative losses in the system. Silicon presents extremely low absorption losses in the considered wavelength range, however absorption and/or scattering losses can be produced by defects or surface roughness during fabrication. Such loss effect is calculated in Fig. 4(b) for the case of mode-1 and $t = 1$ nm by adding an imaginary part k (extinction coefficient) to the silicon refractive index. For $k<10^{-9}$, which is within the results of experimental characterization of Si [53,54], the optical response and the Q-factor value of 2.8×10^6 is not affected. For progressively higher values of the extinction coefficient, the Q-factor deteriorates and the maximum transmittance is reduced due to absorption. The resonance ceases to manifest for $k>10^{-5}$.

Loss mechanisms limit the practically achievable Q-factor due to the introduction of nonradiative losses in the system. In a real scenario, the radiative losses are also bound by the finite lateral size of the MS. The resulting effect has been studied theoretically [55] and experimentally, where the record-high value reported in [36] was measured for a MS with 27×27 cells. A lattice size of 100×100 provides indicatively a safe margin to minimize the finite lattice effect. In the investigated MS this translates to a surface of roughly 0.005 mm^2, which allows for rapid fabrication [56]. Resonance broadening can also be observed due to fabrication tolerances and the resulting statistical variation of the geometrical features among different MS cells. This effect can be as well quantified and taken into account given the fabrication precision [40,57]. Finally, the experimental demonstration of very high Q-factor is also challenging from the standpoint of the measurement setup. For instance, the probing beam should have as low as possible angular dispersion and the detector the necessary spectral resolution. Techniques, such as the cross-polarization resonant scattering spectroscopy, used in the characterization of nanophotonic resonant cavities with Q-factors exceeding one million can provide solutions for the measurement of the MS [58].

The eigenfrequency study of the Q-factor variation in Fig. 4(a) verifies the findings of the RCWA transmittance maps of Fig. 3(d). The Q-factor for mode-2 drops for increasing t down to a value of approximately 1000 for $t = 200$ nm. However, mode-1 shows a finite Q-value local maximum in the order of 10^7 at $t = 116$ nm. In order to provide further insight in this feature, we estimate the coupling strength of the two modes with the incident field as a function of t by calculating the coupling coefficient [48]

$$\gamma_e \propto \iint_A \left(\mathbf{E}_{\text{inc}}^* \times \mathbf{H}_{\text{mode}} + \mathbf{E}_{\text{mode}} \times \mathbf{H}_{\text{inc}}^* \right) \cdot \hat{\mathbf{z}} \, dxdy, \tag{1}$$

where bold symbols refer to the electric and magnetic field vectors of the incident wave and the qBIC modes and $\hat{\mathbf{z}}$ is the unit vector in the plane perpendicular to the metasurface. In the case

here investigated, i.e., for a *y*-polarized impinging planewave, Eq. (1) is simplified as

$$\gamma_e \propto \iint_A \left(\eta_0 H_x + E_y \right) dxdy, \tag{2}$$

where η_0 is the impedance of free space. The integral in Eq. (2) is calculated in the midplane ($z = h/2$) of the slotted rings. The results, shown in Fig. 4(c), corroborate the eigenfrequency analysis, demonstrating a vanishing coupling coefficient at $t = 116$ nm for mode-1. This is further verified by the transmittance spectra calculated in the vicinity of mode-1 resonance for several values of *t* around $t = 116$ nm, which are presented in Fig. 4(d).

The electric field profiles of the two qBIC modes for $t = 116$ nm are shown in Fig. 5. Although the degree of asymmetry along the *y*-axis is not very high, especially in the case of mode-1, the introduction of the silicon bridge perturbs the field distribution leading to reduction of symmetry, since the C_{4v} symmetry of the unperturbed structure is reduced to C_s^y (see Table 4). However, for a critical value of the width *t*, the exact distribution of the electric field leads to minimal coupling with the impinging $\mathbf{E}_y$ planewave, as demonstrated in Fig. 4(c), thus producing a high-*Q* resonance characterized by vanishing transmittance, which can be observed in the spectra of Fig. 4(d) and the transmittance map of Fig. 3(d).

This strong dependence of the mode-1 resonance around $t = 116$ nm on the metasurface geometry, and not its symmetry, is an indication of a resonance-trapped qBIC mode. When the in-plane symmetry of the unit cell in periodic resonant structures is broken, resonance-trapped qBIC modes can appear stemming from the destructive interference of various channels or even from a single resonance [59,60]. Such qBIC modes usually appear at off-Γ conditions, but on-Γ, namely at normal incidence, resonant-trapped modes have also been investigated [61]. The vanishing transmittance on the qBIC resonance is a common characteristic of resonance-trapped modes [41]. Such modes can become pure-BIC by tuning the full set of geometrical parameters in case the symmetry along the *z*-axis is preserved. However, in our case the glass substrate breaks the vertical symmetry of the structure, which leads to finite *Q*-value of the resonance-trapped qBIC. This asymmetry also leads to maximum transmittance of the qBIC resonances slightly lower than 100%, which is a further indication that the resonance-trapped mode cannot become pure BIC [62,63]. Still, the *Q*-factor can obtain values in the order of 10^7, as demonstrated in Fig. 4(a), without the need for very narrow silicon bridges, which is a critical advantage from the fabrication standpoint.

3.3. Diagonal symmetry

Next, we investigate the case of diagonal symmetry with the corresponding MS unit cell structure shown in Fig. 2(d). In that case the symmetry analysis dictates that in the perturbed unit cell the various qBIC modes can be excited by selecting the linear polarization of the incident wave to be parallel or perpendicular to the diagonal plane of symmetry σ_{-xy}. According to Table 5 the target mode-1 (mode-2) is excited when the incident planewave polarization is linear at 45° (135°) with respect to the *x*-axis.

We define the parameter t_d, as in the inset of Fig. 6(a), which describes the width of the silicon wedge placed at the corner of the air slot ring in order to break the symmetry of the structure. The *Q*-factors of the two modes as a function of t_d are calculated by means of eigenfrequency analysis and shown in Fig. 6(a) for values of t_d ranging from 200 nm to 60 nm, namely when $t_d = 2s$ and the silicon inclusion occupies exactly the corner of the slot ring. Contrary to the case of the structure investigated in Fig. 4(a), mode-2 provides higher *Q*-factors. What is more interesting, for the same dimensions of the silicon bridge, that is a block of a square cross-section 30×30 nm², and hence the same fabrication complexity, both modes of the diagonal symmetry structure provide higher *Q*-factors.
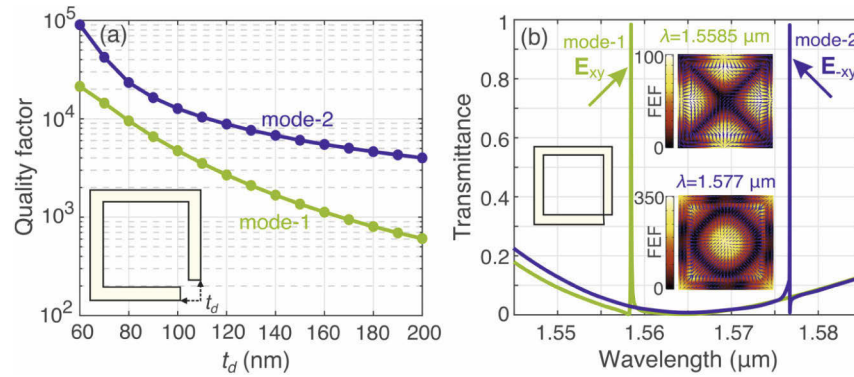
Fig. 6. (a) Quality factor of the two investigated qBIC modes for the case of a perturbed MS unit cell of diagonal symmetry. (b) Transmittance spectra of the MS for two different linear polarizations of the impinging planewave and for t_d = 60 nm. The insets show the profile and enhancement factor of the electric field and the arrow plot of its in-plane components, calculated at the two resonant wavelengths.

The corresponding transmittance spectra for the case t_d = 60 nm are shown in Fig. 6(b) and they show two sharp high-transmittance resonances at 1.5585 μm and 1.557 μm, respectively, for mode-1 and mode-2. The full-wave half-maximum for the mode-1 (mode-2) is $\Delta\lambda$ = 0.072 nm ($\Delta\lambda$ = 0.017 nm), which is in agreement with the corresponding eigenfrequency calculated Q-factors of 21330 (90350). The insets in Fig. 6(b) show the electric field profiles calculated at the resonant wavelengths of the two modes, which confirms that they are the same modes excited in the MS structure with vertical plane of symmetry, as they exhibit the quadrupole and radial profile for mode-1 and mode-2, respectively. The local field enhancement factor is also calculated with a value up to 350 for the more strongly resonant mode-2.

The results in Fig. 6(b) corroborate the findings of the symmetry analysis, namely that by properly selecting the linear polarization of the planewave, the diagonal-symmetry structure allows for EIT effect with a single mode excited, whose Q-factor and wavelength can be adjusted by rotating the MS by 90°. This property can be exploited, for instance, for the design of an EIT-based mechanically switchable sharp passband filter.

We point out that there are several aspects of the discussed metasurfaces, such as the 3D field structure of the possible modes, details of evolution of the modes in the region of small perturbations, dependence of resonances on physical and geometrical parameters of the metasurfaces, etc. They require further investigation and will be presented elsewhere.

4. Refractometric sensing

Finally, we conduct a preliminary assessment of the suitability of the investigated qBIC modes for use as a gas or liquid refractometric sensor by calculating the dependence of mode-1 resonant wavelength on the refractive index of the overlayer material n_o covering the metasurface. Between the two qBIC modes, the first one was selected, as the field profiles of Fig. 5 show that it has stronger interaction with the material inside the slots.

We consider a variation of n_o from 1 to 1.001 (gases) and 1.3 to 1.6 (liquids). The study is limited to the spectral interrogations and the calculation of the bulk refractive index sensitivity $S = \Delta\lambda_{\text{res}}/\Delta n_o$ for t = 1 nm. By inspecting the resulting spectra, shown in Fig. 7, the sensor's figure of merit (FoM) is also estimated as FoM = S/FWHM, namely dividing the bulk sensitivity with full width at half maximum of the resonance linewidth [64]. For the gas- and liquid-sensing scenarios the sensitivities are, respectively, S_g = 57 nm/RIU and S_l = 58.9 nm/RIU.
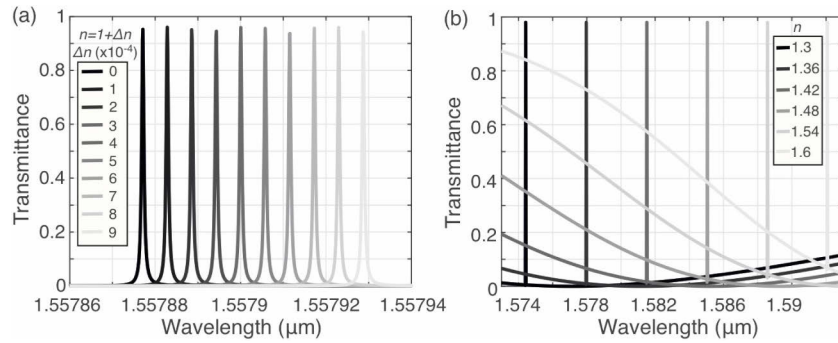
Fig. 7. (a) Transmittance spectra of mode-1 resonance for $t = 1$ nm and various values of the overlayer index for evaluation of the metasurface as gas refractometric sensor. (b) Similar analysis for $1.3 \leq n_o \leq 1.6$ in the context of liquid sensing.

These values are lower than what can be typically achieved in, for instance, plasmonic refractometric sensors based on surface plasmon resonances and/or effects such as extraordinary optical transmission [65]. However, it can be expected that the performance of the proposed sensor can be optimized by increasing the light-matter interaction with the analyte by adjusting the silicon layer thickness and slot width, as well as by working with qBIC modes of the structure with intense field concentration in the slots, such as the quadrupole mode Q_2 in Table 2. Furthermore, the FoM values calculated for the investigated sensor are $\text{FoM}_g = 95 \times 10^3 \text{ RIU}^{-1}$ and $\text{FoM}_l = 117.7 \times 10^3 \text{ RIU}^{-1}$, for gas and liquid sensing, respectively, which are orders of magnitude higher than the state-of-the-art in plasmonic sensors [66], thanks to the small linewidth of the sharp qBIC resonances. Finally, qBIC-based all-dielectric refractometric sensors do not suffer from Ohmic losses, which can potentially lead to thermal heating and damage of the analyte, thus being suitable candidates for refractometric sensors, especially for biosensing [67–70].

5.   Conclusions

In summary, we have proposed a novel silicon-slot dielectric metasurface with an EIT response based on two qBIC modes at normal incidence. By adjusting the structural parameters, the spectral position of these resonances is controlled. Moreover, it was shown that one of the two modes supports a resonance-trapped qBIC, which provides high Q-factors with less stringent fabrication requirements, through the tuning of the metasurface geometry. Finally, the metasurface has been evaluated for use as a refractometric sensor, with the advantage of very high values of FoM, thanks to the strong qBIC resonances. Overall, the proposed structure can find application in systems relying on strong light-matter interactions, such as non-linear devices, biological sensors, or narrowband filtering, e.g., in laser cavities or optical communication systems.

Data availability. Data underlying the results presented in this paper are not publicly available at this time but may be obtained from the authors upon reasonable request.

References

1. S. Liu, A. Vaskin, S. Addamane, B. Leung, M.-C. Tsai, Y. Yang, P. P. Vabishchevich, G. A. Keeler, G. Wang, X. He, Y. Kim, N. F. Hartmann, H. Htoon, S. K. Doorn, M. Zilk, T. Pertsch, G. Balakrishnan, M. B. Sinclair, I. Staude, and I. Brener, "Light-emitting metasurfaces: Simultaneous control of spontaneous emission and far-field radiation," Nano Lett. **18**(11), 6906–6914 (2018).
2. A. Ferraro, D. C. Zografopoulos, M. A. Verschuuren, D. K. G. de Boer, F. Kong, H. P. Urbach, R. Beccherelli, and R. Caputo, "Directional emission of fluorescent dye-doped dielectric nanogratings for lighting applications," ACS Appl. Mater. Interfaces **10**(29), 24750–24757 (2018).
3. A. Arbabi, Y. Horie, M. Bagheri, and A. Faraon, "Dielectric metasurfaces for complete control of phase and polarization with subwavelength spatial resolution and high transmission," Nat. Nanotech. **10**(11), 937–943 (2015).
4. D. C. Zografopoulos, J. F. Algorri, W. Fuscaldo, J. M. López-Higuera, R. Vergaz, J. M. Sánchez-Pena, I.-A. Karolos, R. Beccherelli, V. E. Tsioukas, T. V. Yioultsis, and E. E. Kriezis, "All-dielectric toroidal metasurfaces for angular-dependent resonant polarization beam splitting," Adv. Opt. Mater. **9**(10), 2002143 (2021).
5. A. Tittl, A. Leitis, M. Liu, F. Yesilkoy, D.-Y. Choi, D. N. Neshev, Y. S. Kivshar, and H. Altug, "Imaging-based molecular barcoding with pixelated dielectric metasurfaces," Science **360**(6393), 1105–1109 (2018).
6. J. F. Algorri, D. C. Zografopoulos, A. Ferraro, B. García-Cámara, R. Vergaz, R. Beccherelli, and J. M. Sánchez-Pena, "Anapole modes in hollow nanocuboid dielectric metasurfaces for refractometric sensing," Nanomaterials **9**(1), 30 (2019).
7. D. C. Zografopoulos, J. F. Algorri, A. Ferraro, B. García-Cámara, J. M. Sánchez-Pena, and R. Beccherelli, "Toroidal metasurface resonances in microwave waveguides," Sci. Rep. **9**(1), 7544 (2019).
8. S. Campione, S. Liu, L. I. Basilio, L. K. Warne, W. L. Langston, T. S. Luk, J. R. Wendt, J. L. Reno, G. A. Keeler, I. Brener, and M. B. Sinclair, "Broken symmetry dielectric resonators for high quality factor Fano metasurfaces," ACS Photonics **3**(12), 2362–2367 (2016).
9. J. F. Algorri, D. C. Zografopoulos, A. Ferraro, B. García-Cámara, R. Beccherelli, and J. Sánchez-Pena, "Ultrahigh-quality factor resonant dielectric metasurfaces based on hollow nanocuboids," Opt. Express **27**(5), 6320–6330 (2019).
10. D. C. Zografopoulos and V. Dmitriev, "Quasi-dark resonances in silicon metasurface for refractometric sensing and tunable notch filtering," J. Lightwave Technol. **39**(21), 6985–6993 (2021)..
11. S. Liu, M. B. Sinclair, S. Saravi, G. A. Keeler, Y. Yang, J. Reno, G. M. Peake, F. Setzpfandt, I. Staude, T. Pertsch, and I. Brener, "Resonantly enhanced second-harmonic generation using III-V semiconductor all-dielectric metasurfaces," Nano Lett. **16**(9), 5426–5432 (2016).
12. P. P. Vabishchevich, S. Liu, M. B. Sinclair, G. A. Keeler, G. M. Peake, and I. Brener, "Enhanced second-harmonic generation using broken symmetry III-V semiconductor Fano metasurfaces," ACS Photonics **5**(5), 1685–1690 (2018).
13. C. Yu, H. Tian, Z. Qian, R. Bai, L. Zhu, and Y. Zhang, "Tunable Fano and coupled-resonator-induced transparency resonances in the waveguide-coupled inverted nested ring resonator," Appl. Phys. Express **10**(12), 122202 (2017).
14. Y.-F. Xiao, X.-B. Zou, W. Jiang, Y.-L. Chen, and G.-C. Guo, "Analog to multiple electromagnetically induced transparency in all-optical drop-filter systems," Phys. Rev. A **75**(6), 063833 (2007).
15. C. Sui, B. Han, T. Lang, X. Li, X. Jing, and Z. Hong, "Electromagnetically induced transparency in an all-dielectric metamaterial-waveguide with large group index," IEEE Photonics J. **9**, 1–8 (2017).
16. Y. Ding and R. Magnusson, "Doubly resonant single-layer bandpass optical filters," Opt. Lett. **29**(10), 1135 (2004).
17. Y.-F. Xiao, L. He, J. Zhu, and L. Yang, "Electromagnetically induced transparency-like effect in a single polydimethylsiloxane-coated silica microtoroid," Appl. Phys. Lett. **94**(23), 231115 (2009).
18. W. Liang, L. Yang, J. K. Poon, Y. Huang, K. J. Vahala, and A. Yariv, "Transmission characteristics of a Fabry-Perot etalon-microtoroid resonator coupled system," Opt. Lett. **31**(4), 510 (2006).
19. J. Chen, C. Wang, R. Zhang, and J. Xiao, "Multiple plasmon-induced transparencies in coupled-resonator systems," Opt. Lett. **37**(24), 5133 (2012).
20. H. Lu, X. Gan, D. Mao, B. Jia, and J. Zhao, "Flexibly tunable high-quality-factor induced transparency in plasmonic systems," Sci. Rep. **8**(1), 1558 (2018).
21. Y. Yang, I. I. Kravchenko, D. P. Briggs, and J. Valentine, "All-dielectric metasurface analogue of electromagnetically induced transparency," Nat. Commun. **5**(1), 5753 (2014).
22. R. Singh, I. A. I. Al-Naib, Y. Yang, D. R. Chowdhury, W. Cao, C. Rockstuhl, T. Ozaki, R. Morandotti, and W. Zhang, "Observing metamaterial induced transparency in individual Fano resonators with broken symmetry," Appl. Phys. Lett. **99**(20), 201107 (2011).
23. M. Manjappa, Y. K. Srivastava, and R. Singh, "Lattice-induced transparency in planar metamaterials," Phys. Rev. B **94**(16), 161103 (2016).
24. A. Christofi, Y. Kawaguchi, A. Alù, and A. B. Khanikaev, "Giant enhancement of faraday rotation due to electromagnetically induced transparency in all-dielectric magneto-optical metasurfaces," Opt. Lett. **43**(8), 1838 (2018).
25. B. Han, X. Li, C. Sui, J. Diao, X. Jing, and Z. Hong, "Analog of electromagnetically induced transparency in an E-shaped all-dielectric metasurface based on toroidal dipolar response," Opt. Mater. Express **8**(8), 2197–2207 (2018).

26. J. Diao, B. Han, J. Yin, X. Li, T. Lang, and Z. Hong, "Analogue of electromagnetically induced transparency in an s-shaped all-dielectric metasurface," IEEE Photonics J. **11**(3), 1–10 (2019).

27. N. Papasimakis, V. A. Fedotov, N. I. Zheludev, and S. L. Prosvirnin, "Metamaterial analog of electromagnetically induced transparency," Phys. Rev. Lett. **101**(25), 253903 (2008).

28. S.-Y. Chiam, R. Singh, C. Rockstuhl, F. Lederer, W. Zhang, and A. A. Bettiol, "Analogue of electromagnetically induced transparency in a terahertz metamaterial," Phys. Rev. B **80**(15), 153103 (2009).

29. P. Tassin, L. Zhang, T. Koschny, E. N. Economou, and C. M. Soukoulis, "Planar designs for electromagnetically induced transparency in metamaterials," Opt. Express **17**(7), 5595 (2009).

30. N. Papasimakis, Y. H. Fu, V. A. Fedotov, S. L. Prosvirnin, D. P. Tsai, and N. I. Zheludev, "Metamaterial with polarization and direction insensitive resonant transmission response mimicking electromagnetically induced transparency," Appl. Phys. Lett. **94**(21), 211902 (2009).

31. R. Yahiaoui, J. A. Burrow, S. M. Mekonen, A. Sarangan, J. Mathews, I. Agha, and T. A. Searles, "Electromagnetically induced transparency control in terahertz metasurfaces based on bright-bright mode coupling," Phys. Rev. B **97**(15), 155403 (2018).

32. Y. K. Srivastava, R. T. Ako, M. Gupta, M. Bhaskaran, S. Sriram, and R. Singh, "Terahertz sensing of 7 nm dielectric film with bound states in the continuum metasurfaces," Appl. Phys. Lett. **115**(15), 151105 (2019).

33. L. Cong and R. Singh, "Symmetry-protected dual bound states in the continuum in metamaterials," Adv. Opt. Mater. **7**, 201900383 (2019).

34. C. Kyaw, R. Yahiaoui, J. A. Burrow, V. Tran, K. Keelen, W. Sims, E. C. Red, W. S. Rockward, M. A. Thomas, A. Sarangan, I. Agha, and T. A. Searles, "Polarization-selective modulation of supercavity resonances originating from bound states in the continuum," Commun. Phys. **3**(1), 212 (2020).

35. T. C. Tan, Y. K. Srivastava, R. T. Ako, W. Wang, M. Bhaskaran, S. Sriram, I. Al-Naib, E. Plum, and R. Singh, "Active control of nanodielectric-induced THz quasi-BIC in flexible metasurfaces: a platform for modulation and sensing," Adv. Mater. **33**(27), 2100836 (2021).

36. Z. Liu, Y. Xu, Y. Lin, J. Xiang, T. Feng, Q. Cao, J. Li, S. Lan, and J. Liu, "High-Q quasibound states in the continuum for nonlinear metasurfaces," Phys. Rev. Lett. **123**(25), 253901 (2019).

37. D. R. Abujetas, Á. Barreda, F. Moreno, A. Litman, J.-M. Geffrin, and J. A. Sánchez-Gil, "High-Q transparency band in all-dielectric metasurfaces induced by a quasi bound state in the continuum," Laser Photon. Rev. **15**(1), 2000263 (2020).

38. D. R. Abujetas, Á. Barreda, F. Moreno, J. J. Sáenz, A. Litman, J.-M. Geffrin, and J. A. Sánchez-Gil, "Brewster quasi bound states in the continuum in all-dielectric metasurfaces from single magnetic-dipole resonance meta-atoms," Sci. Rep. **9**(1), 16048 (2019).

39. J. F. Algorri, F. Dell'Olio, P. Roldán-Varona, L. Rodríguez-Cobo, J. M. López-Higuera, J. M. Sánchez-Pena, and D. C. Zografopoulos, "Strongly resonant silicon slot metasurfaces with symmetry-protected bound states in the continuum," Opt. Express **29**(7), 10374 (2021).

40. D. C. Zografopoulos, A. Ferraro, J. F. Algorri, P. Martín-Mateos, B. García-Cámara, A. Moreno-Oyervides, V. Krozer, P. Acedo, R. Vergaz, J. M. Sánchez-Pena, and R. Beccherelli, "All-dielectric silicon metasurface with strong subterahertz toroidal dipole resonance," Adv. Opt. Mater. **7**(19), 1900777 (2019).

41. S. Han, L. Cong, Y. K. Srivastava, B. Qiang, M. V. Rybin, A. Kumar, R. Jain, W. X. Lim, V. G. Achanta, S. S. Prabhu, Q. J. Wang, Y. S. Kivshar, and R. Singh, "All-dielectric active terahertz photonics driven by bound states in the continuum," Adv. Mater. **31**(37), 1901921 (2019).

42. J. Jeong, M. D. Goldflam, S. Campione, J. L. Briscoe, P. P. Vabishchevich, J. Nogan, M. B. Sinclair, T. S. Luk, and I. Brener, "High quality factor toroidal resonances in dielectric metasurfaces," ACS Photonics **7**(7), 1699–1707 (2020).

43. M. Wu, S. T. Ha, S. Shendre, E. G. Durmusoglu, W.-K. Koh, D. R. Abujetas, J. A. Sánchez-Gil, R. Paniagua-Domínguez, H. V. Demir, and A. I. Kuznetsov, "Room-temperature lasing in colloidal nanoplatelets via Mie-resonant bound states in the continuum," Nano Lett. **20**(8), 6005–6011 (2020).

44. M. Qin, S. Xiao, W. Liu, M. Ouyang, T. Yu, T. Wang, and Q. Liao, "Strong coupling between excitons and magnetic dipole quasi-bound states in the continuum in WS$_2$-TiO$_2$ hybrid metasurfaces," Opt. Express **29**(12), 18026–18036 (2021).

45. C. J. Bradley and A. P. Cracknell, *The Mathematical Theory of Symmetry in Solids: Representation Theory for Point Groups and Space Groups*, Oxford Classic Texts in the Physical Sciences (Oxford University Press Inc., New York, 2009).

46. A. A. Barybin and V. A. Dmitriev, *Modern Electrodynamics and Coupled-Mode Theory: Application to Guided-Wave Optics*, (Rinton Press Princeton, New Jersey, (2002).

47. A. Nussbaum, "Group theory and normal modes," Am. J. Phys. **36**(6), 529–539 (1968).

48. A. C. Overvig, S. C. Malek, M. J. Carter, S. Shrestha, and N. Yu, "Selection rules for quasibound states in the continuum," Phys. Rev. B **102**(3), 035434 (2020).

49. V. Dmitriev, S. D. S. Santos, A. S. Kupriianov, and V. R. Tuz, "Transition between toroidic orders in dielectric metasurfaces by polarization of the incident wave," Opt. Lett. **46**(12), 2964–2967 (2021).

50. P. Lalanne and G. M. Morris, "Highly improved convergence of the coupled-wave method for TM polarization," J. Opt. Soc. Am. A **13**(4), 779 (1996).

51. P. Lalanne and M. P. Jurek, "Computation of the near-field pattern with the coupled-wave method for transverse magnetic polarization," J. Mod. Opt. **45**(7), 1357–1374 (1998).

52. J. Jiang, R. Lupoiu, E. W. Wang, D. Sell, J. P. Hugonin, P. Lalanne, and J. A. Fan, "MetaNet: a new paradigm for data sharing in photonics research," Opt. Express **28**(9), 13670 (2020).

53. M. A. Green, "Self-consistent optical parameters of intrinsic silicon at 300 K including temperature coefficients," Sol. Energy Mater Sol. **92**(11), 1305–1310 (2008).

54. C. Schinke, P. C. Peest, J. Schmidt, R. Brendel, K. Bothe, M. R. Vogt, I. Kröger, S. Winter, A. Schirmacher, S. Lim, H. T. Nguyen, and D. MacDonald, "Uncertainty analysis for the coefficient of band-to-band absorption of crystalline silicon," AIP Adv. **5**(6), 067168 (2015).

55. V. I. Zakomirnyi, A. E. Ershov, V. S. Gerasimov, S. V. Karpov, H. Ågren, and I. L. Rasskazov, "Collective lattice resonances in arrays of dielectric nanoparticles: a matter of size," Opt. Lett. **44**(23), 5743 (2019).

56. K. Li, J. Li, C. Reardon, C. S. Schuster, Y. Wang, G. J. Triggs, N. Damnik, J. Müenchenberger, X. Wang, E. R. Martins, and T. F. Krauss, "High speed e-beam writing for large area photonic nanostructures - a choice of parameters," Sci. Rep. **6**(1), 32945 (2016).

57. J. Kühne, J. Wang, T. Weber, L. Kühner, S. A. Maier, and A. Tittl, "Fabrication robustness in BIC metasurfaces," Nanophotonics **10**(17), 4305–4312 (2021).

58. Y. Lai, S. Pirotta, G. Urbinati, D. Gerace, M. Minkov, V. Savona, A. Badolato, and M. Galli, "Genetically designed L3 photonic crystal nanocavities with measured quality factor exceeding one million," Appl. Phys. Lett. **104**(24), 241101 (2014).

59. C. W. Hsu, B. Zhen, A. D. Stone, J. D. Joannopoulos, and M. Soljačić, "Bound states in the continuum," Nat. Rev. Mater. **1**(9), 16048 (2016).

60. S. Han, P. Pitchappa, W. Wang, Y. K. Srivastaca, M. V. Rybin, and R. Singh, "Extended bound states in the continuum with symmetry-broken terahertz dielectric metasurfaces," Adv. Opt. Mater. **9**(7), 2002001 (2021).

61. A. I. Ovcharenko, C. Blanchard, J.-P. Hugonin, and C. Sauvan, "Bound states in the continuum in symmetric and asymmetric photonic crystal slabs," Phys. Rev. B **101**(15), 155303 (2020).

62. C. W. Hsu, B. Zhen, J. Lee, S.-L. Chua, S. G. Johnson, J. D. Joannopoulos, and M. Soljačić, "Observation of trapped light within the radiation continuum," Nature **499**(7457), 188–191 (2013).

63. A. Taghizadeh, J. Mørk, and I.-S. Chung, "Ultracompact resonator with high quality-factor based on a hybrid grating structure," Opt. Express **23**(11), 14913–14921 (2015).

64. Y. Xu, P. Bai, X. Zhou, Y. Akimov, C. E. Png, L.-K. Ang, W. Knoll, and L. Wu, "Optical refractive index sensors with plasmonic and photonic structures: Promising and inconvenient truth," Adv. Opt. Mater. **7**(9), 1801433 (2019).

65. W. Yue, Z. Wang, Y. Yang, J. Li, Y. Wu, L. Chen, B. Ooi, X. Wang, and X.-X. Zhang, "Enhanced extraordinary optical transmission (EOT) through arrays of bridged nanohole pairs and their sensing applications," Nanoscale **6**(14), 7917 (2014).

66. B. Liu, S. Chen, J. Zhang, X. Yao, J. Zhong, H. Lin, T. Huang, Z. Yang, J. Zhu, S. Liu, C. Lienau, L. Wang, and B. Ren, "A plasmonic sensor array with ultrahigh figures of merit and resonance linewidths down to 3 nm," Adv. Mater. **30**(12), 1706031 (2018).

67. S. Romano, G. Zito, S. Torino, G. Calafiore, E. Penzo, G. Coppola, S. Cabrini, I. Rendina, and V. Mocella, "Label-free sensing of ultralow-weight molecules with all-dielectric metasurfaces supporting bound states in the continuum," Opt. Express **6**, 726–733 (2018).

68. S. Romano, G. Zito, S. N. L. Yépez, S. Cabrini, E. Penzo, G. Coppola, I. Rendina, and V. Mocella, "Tuning the exponential sensitivity of a bound-state-in-continuum optical sensor," Opt. Express **27**(13), 18776–18786 (2019).

69. A. Ndao, L. Hsu, W. Cai, J. Ha, J. Park, R. Contractor, Y. Lo, and B. Kanteé, "Differentiating and quantifying exosome secretion from a single cell using quasi-bound states in the continuum," Nanophotonics **9**(5), 1081–1086 (2020).

70. Y. Jahani, E. R. Arvelo, F. Yesilkoy, K. Koshelev, C. Cianciaruso, M. De Palma, Y. Kivshar, and H. Altug, "Imaging-based spectrometer-less optofluidic biosensors based on dielectric metasurfaces for detecting extracellular vesicles," Nat. Commun. **12**(1), 3246 (2021).